



## Research paper

Efficient photocatalytic hydrogen production over La/Rh co-doped Ruddlesden-Popper compound  $\text{Sr}_2\text{TiO}_4$ 

Xiaoqin Sun, Xiaoxiang Xu\*

Shanghai Key Lab. of Chemical Assessment and Sustainability, School of Chemical Science and Engineering, Tongji University, 1239 Siping Road, Shanghai 200092, China

## ARTICLE INFO

## Article history:

Received 1 February 2017

Received in revised form 17 March 2017

Accepted 24 March 2017

Available online 27 March 2017

## Keywords:

Photocatalyst

Hydrogen production

Ruddlesden-Popper compound

Rh doping

DFT calculation

## ABSTRACT

Layered semiconductor compounds often exhibit intriguing properties for photocatalytic water splitting, probably correlated with their peculiar crystal structures that facilitate charge separations. In this work, we perform an investigation on the layered Ruddlesden-Popper compound  $\text{Sr}_2\text{TiO}_4$  and its La/Rh co-doped counterparts for photocatalytic hydrogen production from water. Their crystal structures, optical absorption and other physicochemical properties have been systematically explored. Our results suggest that La/Rh can be successfully incorporated into  $\text{Sr}_2\text{TiO}_4$  with layered crystal structure maintained. The use of polymerized-complex method for sample synthesis significantly reduces the calcination temperature as low as 900 °C. La/Rh serves as efficient dopants for extending the light absorbance of  $\text{Sr}_2\text{TiO}_4$  as far as 550 nm. Photocatalytic hydrogen productions are also considerably improved after La/Rh co-doping under both full range ( $\lambda \geq 250$  nm) and visible light irradiation ( $\lambda \geq 420$  nm). An optimal doping level is reached at 3% ( $\text{Sr}_{1.97}\text{La}_{0.03}\text{Ti}_{0.97}\text{Rh}_{0.03}\text{O}_4$ ) which gives the highest average hydrogen production rate  $\sim 100 \mu\text{mol}/\text{h}$  and  $\sim 40 \mu\text{mol}/\text{h}$  under full range ( $\lambda \geq 250$  nm) and visible light irradiation ( $\lambda \geq 420$  nm), corresponding to apparent quantum efficiency  $\sim 1.27\%$  and  $\sim 1.18\%$ , respectively. Photoelectrochemical analysis reveals that charge separation and electron lifetime strongly depends on the level of La/Rh co-doping. Mott-Schottky analysis and theoretical calculations indicate that the improved light absorption of La/Rh co-doped  $\text{Sr}_2\text{TiO}_4$  stems from the formation of new valence band with Rh 4d character which uplifts the valence band edge of  $\text{Sr}_2\text{TiO}_4$ .

© 2017 Elsevier B.V. All rights reserved.

## 1. Introduction

How to balance the ever-growing energy needs of our modern society has been an urgent task, not only because we are jeopardized by a severe shortage of fossil fuels, but also due to various environmental problems associated with fossil fuel usage [1–3]. In these contexts, there is now a growing consensus on searching clean and renewable energy resources and/or developing affordable green energy technologies that can decarbonize our fossil fuel-based economy [4]. Photocatalytic hydrogen production from water, driven by solar insolation, offers a promising resolution to above issues [5–17]. This is because hydrogen is a clean energy vector in photocatalysis whose utilization and generation involve only water and also because solar energy is inexhaustible in nature and widely accessible all over the world [3,18]. The practical deployment of this tempting technique has been largely

hampered by the low solar to hydrogen efficiency (STH) of current photocatalysts [19,20]. Such a low STH at least partly originates from a poor absorption of solar spectrum as most of photocatalysts are wide band gap semiconductors whose band gaps are too large to harvest appreciable amounts of solar energy [21,22]. Thereby, band gap management of semiconductors serves as a premier target for the development of efficient photocatalysts. For example, reducing the band gap of a semiconductor from 3.2 eV to 2.0 eV enormously increases the theoretical STH from less than 1%–16% [19]. In this regard, doping techniques have been frequently adopted to tailor the light absorption of various wide band gap semiconductors [23–28]. These mainly refer to the introduction of foreign atoms into the crystal structures of these semiconductors whereby additional energy states/bands are induced so as to reduce the threshold of light absorption. Take  $\text{SrTiO}_3$  ( $E_g = 3.2$  eV) as an example, by using different doping strategies, i.e. Cr doping [29,30], Ni/Nb co-doping [31], Bi/Cr co-doping [32] and La/N co-doping [33] etc.,  $\text{SrTiO}_3$  demonstrates interesting photocatalytic properties under visible light illumination. Among various doping elements for  $\text{SrTiO}_3$ , Rh serves as one of the most efficient dopants with

\* Corresponding author.

E-mail addresses: [xxxu@tongji.edu.cn](mailto:xxxu@tongji.edu.cn), [xiaoxiangx@gmail.com](mailto:xiaoxiangx@gmail.com) (X. Xu).

quantum yield approaching 5.2% at 420 nm for H<sub>2</sub> production from water [34]. However, Rh doped SrTiO<sub>3</sub> often contains detrimental Rh<sup>4+</sup> species and/or oxygen vacancies due to a charge compensation phenomenon, which greatly suppress the photocatalytic performance [34–36]. This has been solved by co-doping La along with Rh to build a charge balanced system in SrTiO<sub>3</sub> [37]. Indeed, recent studies on La/Rh co-doped SrTiO<sub>3</sub> have witnessed a number of successes in whole water splitting through a Z-scheme setup [38–40]. Although there have been numerous studies on the compositional modification to SrTiO<sub>3</sub>, studies on its layered derivative Sr<sub>2</sub>TiO<sub>4</sub> are generally lacking. Previously, we investigated La/Cr co-doped Sr<sub>2</sub>TiO<sub>4</sub>, which demonstrated interesting photocatalytic activity for hydrogen production from water under visible light irradiation [41]. The similar ionic size of Rh<sup>3+</sup> and Cr<sup>3+</sup> in octahedral coordination yet much larger dispersity of Rh 4d orbital than Cr 3d orbital implies that Rh might be a good dopant for Sr<sub>2</sub>TiO<sub>4</sub> in terms of extending visible light absorption and improving photocatalytic activity. Previous studies on simple perovskite SrTiO<sub>3</sub> suggest that Rh doping effectively tunes the semiconductivity of SrTiO<sub>3</sub> from n-type to p-type [42]. Whether the same phenomenon occurs in Sr<sub>2</sub>TiO<sub>4</sub> needs to be confirmed. Besides, there are remaining questions to be answered in these doping systems such as the existence of optimal doping level and possible low temperature synthetic route etc. Here we perform an investigation on the low temperature synthesized layered perovskite Sr<sub>2</sub>TiO<sub>4</sub> and its La/Rh co-doped counterparts for photocatalytic water splitting. Layered perovskite Sr<sub>2</sub>TiO<sub>4</sub> (n=1) is one of the end members to the Ruddlesden-Popper (RP) series Sr<sub>n+1</sub>Ti<sub>n</sub>O<sub>3n+1</sub> (1≤n≤∞) whose crystal structures strongly correlate to SrTiO<sub>3</sub> (n=∞) by structural lamination along c axis [43,44]. Recent studies have pointed out that the surface of perovskite type compounds is essentially of relevant RP series structures [45–47]. It is therefore of high necessity to examine the RP type compounds for a better understanding of perovskite photocatalysis as all photocatalytic reactions proceed at the surface.

## 2. Experimental

### 2.1. Material synthesis

All samples with nominal chemical formula Sr<sub>2-x</sub>La<sub>x</sub>Ti<sub>1-x</sub>Rh<sub>x</sub>O<sub>4</sub> (x=0, 0.01, 0.03 and 0.05) were synthesized by standard polymerized-complex method: appropriate amounts of titanium isopropanol (Aladdin, 95%), citric acid (Aladdin, 99.5%), strontium nitrate (SCR, 99.5%), lanthanum nitrate (Aladdin, 99%) and rhodium chloride trihydrate (HWRK, 98%) were dissolved into ethylene glycol (Aladdin, GC grade) with the aid of deionized water. The solution was magnetically stirred at 423 K until a transparent gel was formed and heated at 573 K for 2 h to promote polymerization. The resultant brown resin was then calcined at 823 K for 5 h to remove organic species and was ground into powders. The powders were uniaxially pressed into pellets under a pressure of 5 tons and were calcined at 1173 K for 10 h in a muffle furnace. The calcined pellets were then ground into powders and were collected for further analysis. Pristine Sr<sub>2</sub>TiO<sub>4</sub> (x=0), mildly La/Rh co-doped Sr<sub>2</sub>TiO<sub>4</sub> (x=0.005) and La or Rh singly doped Sr<sub>2</sub>TiO<sub>4</sub> were also synthesized under the same conditions.

### 2.2. Methods for analysis

Crystal structure and phase purity was checked by X-ray diffraction (XRD) techniques on a Bruker D8 Focus diffractometer. Incident radiation was Cu K<sub>α1</sub> ( $\lambda$ =1.5406 Å) and Cu K<sub>α2</sub> ( $\lambda$ =1.5444 Å). The step size for data collection was 0.02° with a collection time 10 s at each step. Crystal structure analysis and simulation was performed

by Rietveld refinement method using the General Structure Analysis System (GSAS) software package [48,49]. Diffuse reflectance spectra were collected using a UV-vis spectrometer (JASCO-V750) and were analyzed using JASCO software suite. BaSO<sub>4</sub> was used as a non-absorbing reference material [50]. The morphology of the samples was inspected under a field emission scanning electron microscope (Hitachi S4800) and a transmission electron microscope (JEOL JEM-2100). Surface chemical compositions and binding energy of individual elements were analyzed using X-ray photoelectron spectroscopy (AXIS Ultra DLD with a monochromatic Al K $\alpha$  X-ray source). The adventitious carbon C 1s peak at 284.7 eV was used as a reference to the binding energy of individual core level state [51]. Compositions of as-prepared samples were analyzed by inductively coupled plasma techniques (ICP) (Perkin-Elmer PE Optima 2100 DV). Surface areas were analyzed on a Micro-meritics instrument TriStar 3000 and were calculated via the Brunauer-Emmett-Teller (BET) model.

### 2.3. Photocatalytic hydrogen production

The hydrogen evolution reactions of Sr<sub>2</sub>TiO<sub>4</sub> and La/Rh co-doped ones were carried out in a top-irradiation-type reactor connected to a gas-closed circulation and evacuation system (Perfect Light, Lab solar-IIIAG). Water jacket was used to stabilize the reactor temperature around 20 °C. In a typical experiment, 100 mg sample powders were ultrasonically dispersed into 100 mL Na<sub>2</sub>SO<sub>3</sub> aqueous solution (0.05 M), which was then sealed and evacuated in the reactor. The gas pressure inside the reactor is typically 100 Pa. 1 wt% Pt was applied as a co-catalyst and was deposited onto the sample powders by thermal deposition method [26,52–54]: proper amounts of H<sub>2</sub>PtCl<sub>6</sub> aqueous solution were impregnated into sample powders. The slurry formed was heated on a hot-plate at 90 °C until dry and calcined at 180 °C for 2 h to fully decompose H<sub>2</sub>PtCl<sub>6</sub> into Pt nanoparticles. A 500 W high-pressure mercury lamp (NBeT, Merc-500) was used as the light source. Visible light was generated by filtering the output of the lamp with a UV cut-off filter ( $\lambda$ ≥420 nm). The photon flux of the lamp is calibrated using a quantum meter (Apogee MP-300). The recorded photon flux is ~1543.9  $\mu\text{mol m}^{-2} \text{s}^{-1}$  for full range irradiation ( $\lambda$ ≥250 nm) and ~668.5  $\mu\text{mol m}^{-2} \text{s}^{-1}$  for visible light irradiation ( $\lambda$ ≥420 nm). The Gas composition within the reactor was analyzed by an online gas chromatography (TECHCOMP, GC7900 with a TCD detector, argon carrier gas). The apparent quantum efficiency is then calculated using the following equation:

$$\text{Apparent quantum efficiency} = 2 \times \text{mol of hydrogen production per hour} / \text{mole of photon flux per hour} \times 100\%$$

### 2.4. Photoelectrochemical measurements

Photoelectrodes of as-prepared samples were fabricated by an electrophoretic deposition method [55,56]: two pieces of fluorine doped tin oxide (FTO) glass (30×10 mm) were immersed into 50 mL acetone solution containing 50 mg sample powders and 10 mg iodine. The two pieces of glass were kept in parallel with a 10 mm separation and the conductive sides facing inward. A constant bias (15 V) was applied between the two pieces of glass for 10 min under potentiostatic control (Keithley 2450 Source Meter). The prepared electrodes were then calcined at 473 K for 10 min to remove absorbed iodine. A TiCl<sub>4</sub> (Alfa-Aesar, 99.9%) methanol solution (10 mM) was dropped onto the electrode and dried in air. The same procedure was repeated six times to minimize the exposure of naked FTO. The electrode was then calcined under a nitrogen flow (20 mL min<sup>-1</sup>) at 673 K for 1 h. Photoelectrochemical measurements were performed with a three-electrode configuration setup using a Zahner electrochemical workstation. The sample photoelectrode, Pt foil (10×10 mm) and Ag/AgCl electrode were

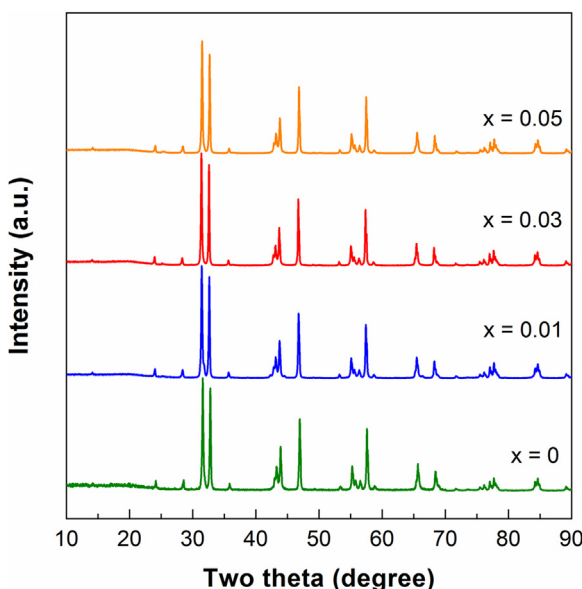


**Fig. 1.** X-ray powder diffraction patterns of freshly prepared samples  $\text{Sr}_{2-x}\text{Lax}\text{Ti}_{1-x}\text{Rh}_x\text{O}_4$  ( $x = 0, 0.01, 0.03$  and  $0.05$ ).

used as the working, counter and reference electrodes, respectively. An aqueous solution of  $\text{K}_3\text{PO}_4/\text{K}_2\text{HPO}_4$  (0.1 M, pH = 7.95) was used as an electrolyte and a buffer.  $\text{Na}_2\text{SO}_3$  (0.05 M) was added to the solution as a hole scavenger. A 300 W Xenon lamp (Perfect Light, PLX-SXE300) coupled with a UV cutoff filter ( $\lambda \geq 420$  nm) was applied as the light source. The incident light was rectified by an electronic timer and shutter (DAHENG, GCI-73).

## 2.5. Theoretical calculations

Theoretical calculations were performed using the density functional theory (DFT) through the Vienna Ab initio Simulation Package (VASP) [57]. The Perdew, Burke and Ernzerhof (PBE) exchange-correlation functional within the generalized gradient approximation (GGA) [58] and the projector augmented-wave pseudo potential were applied [59]. A  $2 \times 2 \times 1$  super cell ( $a = b = 7.77$  Å,  $c = 12.60$  Å,  $\alpha = \beta = \gamma = 90^\circ$ ) was constructed for calculation. La/Rh co-doping was simulated by replacing 1 Sr and 1 Ti with 1 La and 1 Rh randomly. All geometry structures were fully relaxed until the forces on each atom are less than 0.01 eV/Å. Static calculations were performed with a  $8 \times 8 \times 5$  Monkhorst-Pack  $k$ -point grid [60].

## 3. Results and discussions

### 3.1. Phase purity and crystal structure

The synthesis of Ruddlesden-Popper compound  $\text{Sr}_2\text{TiO}_4$  was normally carried out at high temperatures ( $\geq 1100$  °C) and is likely due to the high energy barrier for the insertion of  $\text{SrO}$  layers into perovskite structure of  $\text{SrTiO}_3$  [61–63]. High temperature calcination is generally unfavorable for the preparation of photocatalytic materials as it strongly promotes particle growth and reduces surface area [64]. In this work, we use a polymerized-complex (PC) method for the preparation of  $\text{Sr}_2\text{TiO}_4$  and its doped counterparts. The homogeneous dispersion of all reactants at atomic level in PC method before calcination would ease atom rearrangement thereby significantly lower the level of thermal treatment needed for phase formation. Indeed, we were able to synthesize this refractory compound at a calcination temperature as low as 900 °C. Fig. 1 illustrates the X-ray powder diffraction patterns for

the freshly prepared samples. All these patterns can be indexed using a tetragonal symmetry, indicative of a single phase. Both pristine and doped  $\text{Sr}_2\text{TiO}_4$  exhibit sharp diffraction peaks, suggesting a good crystallinity. We then performed the Rietveld refinement on all XRD data using a tetragonal lattice (space group  $I\ 4/mmm$ ) and those refined unit cell parameters are tabulated in Table 1. A typical refined XRD patterns for  $\text{Sr}_{1.97}\text{La}_{0.03}\text{Ti}_{0.97}\text{Rh}_{0.03}\text{O}_4$  ( $x = 0.03$ ) is displayed in Fig. 2. Reasonable goodness-of-fit parameters ( $R_p$ ,  $R_{wp}$  and  $\chi^2$ ) were achieved only by placing constraints that Sr/La and Ti/Rh dwell on the same crystallographic position, respectively. Therefore, La and Rh have been successfully doped into the crystal structure of  $\text{Sr}_2\text{TiO}_4$ . The incorporation of La/Rh into  $\text{Sr}_2\text{TiO}_4$  crystal lattice can be further verified by the gradual expansion of unit cells along with La/Rh co-doping (Table 1). This can be explained by the substitution of small  $\text{Ti}^{4+}$  cations (ionic radius  $r_{\text{Ti}}^{4+} = 0.605$  Å in octahedral symmetry) with large  $\text{Rh}^{3+}$  cations (ionic radius  $r_{\text{Rh}}^{3+} = 0.665$  Å in octahedral symmetry) according to Vegard's law [65,66]. The substitution of Sr/Ti with La/Rh is likely to be random as super-lattice peaks for cation ordering is not detected. The homogeneity of these dopants in  $\text{Sr}_2\text{TiO}_4$  was further verified by high resolution TEM (Fig. S1) and EDS mapping analysis (Fig. S2), where impurities or phase segregations were not detected. A schematic representation of the refined crystal structure is illustrated in Fig. 2 (inserted image). The crystal structure of RP compound is dissimilar to ideal perovskite by laminating along  $c$  axis, which in turn breaks the connectivity of  $\text{TiO}_6$  octahedrons along  $c$  direction. Such a disconnection between up and low O-Ti-O network shall have profound impacts on the electronic structures as charge migrations occur dominantly through this network [67,68]. For singly doped  $\text{Sr}_2\text{TiO}_4$ , single phase compound was only achieved in Rh doped  $\text{Sr}_2\text{TiO}_4$  (3% Rh doping) and impurity peaks assignable to  $\text{La}_2\text{O}_3$  was clearly seen in XRD patterns of La singly doped  $\text{Sr}_2\text{TiO}_4$  (Fig. S4a). The composition of these samples was then analyzed by ICP techniques which suggest cation ratios commensurate to the nominal chemical formula. Thereby, we have successfully prepared a series of La/Rh co-doped  $\text{Sr}_2\text{TiO}_4$  at low calcination temperatures.

### 3.2. Microstructures

Microstructures are important parameters relevant to photocatalytic performance [52,56,69,70]. The microstructures of as-prepared samples were examined using a field emission scanning electron microscopy (FESEM). Fig. 3 displays typical FESEM images of all samples. As can be seen from Fig. 3, particles of all samples are composed of agglomeration of small grains. The typical grain size is around 200 nm, which is considerably smaller than those prepared from solid state reactions [41]. Such a small grain size is highly beneficial for photocatalytic reactions, not only because of a large surface area hence more reaction sites but also due to a short charge migration pathway from bulk to the surface. We own these microstructures to the low calcination temperatures (900 °C) where substantial grain growth is prohibited. Accordingly, all samples demonstrate comparable surface area according to BET analysis (Table 1). La/Rh co-doping seems to favor a large surface area as can be seen from those smaller granules in FESEM at high doping levels (Fig. 3d).

### 3.3. UV-vis spectroscopy

The color of pristine  $\text{Sr}_2\text{TiO}_4$  is white, confirming a wide band gap semiconductor. Interestingly, introducing merely 1% Rh into  $\text{Sr}_2\text{TiO}_4$  effectively turns the color from white to yellow, as can be seen from the digital photo of sample powders in Fig. 4. Such a strong yellowish color suggests substantial visible light absorption thereby Rh serves as an efficient dopant for extending light absorption of  $\text{Sr}_2\text{TiO}_4$ . Fig. 4 illustrate the UV-vis absorption spectra of all

**Table 1**

Unit cell parameters, BET surface area and band gap values of as-prepared samples  $\text{Sr}_{2-x}\text{La}_x\text{Ti}_{1-x}\text{Rh}_x\text{O}_4$  ( $x = 0, 0.01, 0.03$  and  $0.05$ ), standard deviation is specified in the parenthesis.

x	Space group	$a/\text{\AA}$	$c/\text{\AA}$	$V/\text{\AA}^3$	BET surface area ( $\text{m}^2/\text{g}$ )	Band gap (eV)
0	$I\bar{4}/mmm$	3.8841(1)	12.5867(2)	189.89(1)	4.9	3.49(3)
0.01	$I\bar{4}/mmm$	3.8856(1)	12.5831(3)	189.99(1)	4.5	2.43(1)
0.03	$I\bar{4}/mmm$	3.8864(1)	12.5891(2)	190.15(1)	6.8	2.43(1)
0.05	$I\bar{4}/mmm$	3.8869(1)	12.5958(3)	190.25(1)	9.9	2.41(1)

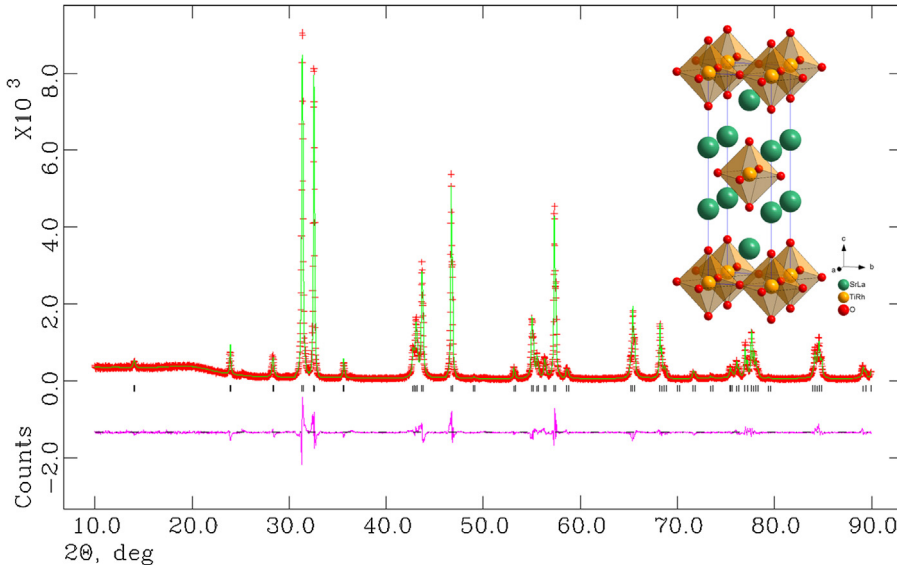


**Fig. 2.** Observed and calculated X-ray powder diffraction patterns of  $\text{Sr}_{1.97}\text{La}_{0.03}\text{Ti}_{0.97}\text{Rh}_{0.03}\text{O}_4$  ( $x = 0.03$ ). The refinements converged with good  $R$  and  $\chi^2$  factor ( $R_p = 11.87\%$ ,  $R_{wp} = 8.98\%$ ,  $\chi^2 = 3.978$ ). Schematic representation of refined crystal structure is shown as inserted image.

samples, which are converted from diffuse reflectance spectra. Pristine  $\text{Sr}_2\text{TiO}_4$  exhibit a sharp absorption edge below 400 nm, being consistent with its white color and wide band gap. On the contrary, the absorption edge is clearly red-shifted in La/Rh co-doped samples, extending deeply into visible light region ( $\sim 550$  nm) and contributing to their colored appearance. Interestingly, the doping level from 1% to 5% simply enhances the absorbance between 350 nm to 500 nm but has little impact towards absorbance above 500 nm. The absorption band between 350 nm and 500 nm have been frequently assigned to charge-transfer excitations from  $\text{Rh}^{3+}$  to  $\text{Ti}^{4+}$  and are responsible for visible light photocatalytic activity [27,34,71,72]. Presumably, a higher level of Rh doping would enhance these excitations, which explains the trend in light absorption. This is further confirmed by samples at mild doping level ( $x = 0.005$ ) which clearly shows decreased visible light absorption compared with high doping levels (Fig. S3). More importantly, Rh with high oxidation state (e.g.  $\text{Rh}^{4+}$  species) often induces an absorption peak centered at around 600 nm and turns sample powders into a violet color [34,71]. This has been reported in a number of Rh doped systems where charge is not properly compensated [71,73–75]. Similar phenomenon is also observed here in Rh singly doped  $\text{Sr}_2\text{TiO}_4$  (3% Rh doping), which clearly shows intensive absorption band at 600 nm. The absence of this absorption band and yellowish sample color in La/Rh co-doped  $\text{Sr}_2\text{TiO}_4$  suggest suppression of these species. The role of La in these co-doped systems can be understood as to balance the charge during replacement of  $\text{Ti}^{4+}$  with  $\text{Rh}^{3+}$  since doping La alone does not even gain a single phase compound and sample powders remain a white color (Fig. S4). High oxidation state Rh species are generally detrimental to photocatalytic activity as they would competitively consume photo-generated electrons [34]. Therefore, by co-doping La with Rh, we have managed to balance the charge in  $\text{Sr}_2\text{TiO}_4$  and avoid high

oxidation state Rh species. Band gap of pristine and La/Rh co-doped  $\text{Sr}_2\text{TiO}_4$  were determined by Kubelka-Munk transforming diffuse reflectance data and extrapolating the absorption edge down to the energy axis. These results are tabulated in Table 1. Pristine  $\text{Sr}_2\text{TiO}_4$  owns a band gap around 3.5 eV while all doped samples have similar band gap value of 2.4 eV. These values are all comparable to other Rh doped systems [27,34,75].

### 3.4. X-ray photoelectron spectroscopy (XPS)

The surface nature of freshly prepared samples was analyzed by using X-ray photoelectron spectroscopy (XPS) techniques. Binding energies of core-level electrons from constituent elements La, Ti, Rh, and O are shown in Fig. 5. All signals were referenced to C 1s peak centered at 284.7 eV, arising from adventitious carbon. Overlapping peaks were unfolded by fitting with different Gaussian functions. The Ti 2p states of all samples involve two peaks centered at 457.7 eV and 463.5 eV, assignable to  $\text{Ti} 2p_{3/2}$  and  $\text{Ti} 2p_{1/2}$  states of  $\text{Ti}^{4+}$  species, respectively [41,76]. The O 1s states typically show two overlapping peaks at around 531 eV and 529 eV, attributed to surface OH groups and lattice oxygen [77,78]. Presumably, the surface of these samples is highly hydrophilic as indicated by the strong peaks for OH groups. The signals for La 3d states are only detectable for samples with high doping levels, i.e.  $x = 0.03$  and  $0.05$ . Two peaks centered at around 833 eV and 850 eV are discernable, corresponding to  $3d_{5/2}$  and  $3d_{3/2}$  states due to spin-orbital splitting [76]. Shoulders at higher binding energy typically belong to charge transfer shake-up satellites [79]. Likewise, Rh 3d signals are only observed for heavily doped samples with two separated peaks at around 309 eV and 314 eV, assignable to  $3d_{5/2}$  and  $3d_{3/2}$  states of  $\text{Rh}^{3+}$  species [27]. Signals for high oxidation state Rh (e.g.  $\text{Rh}^{4+}$ )

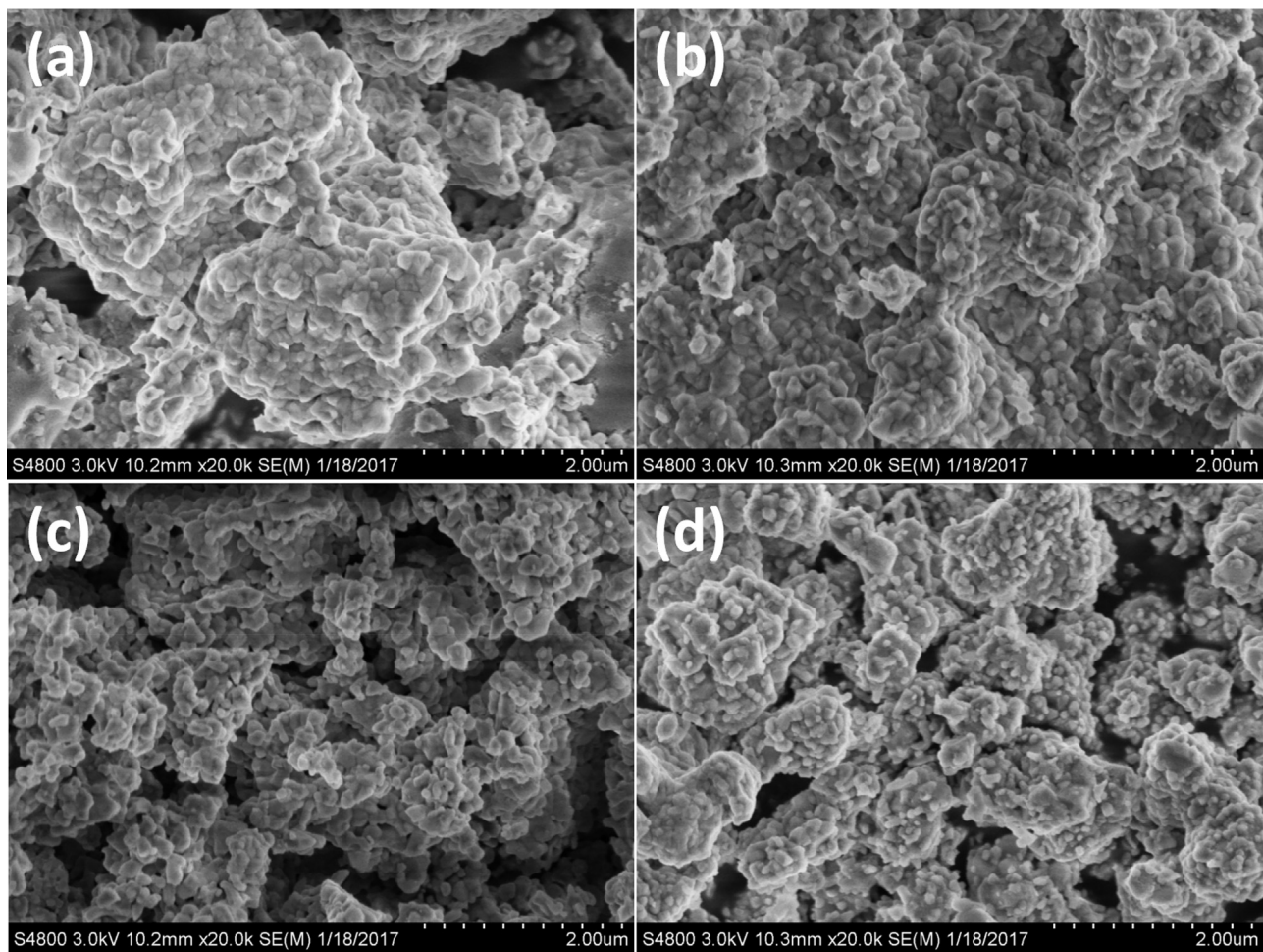


**Fig. 3.** Field emission scanning electron microscopy images of freshly prepared samples  $\text{Sr}_{2-x}\text{La}_x\text{Ti}_{1-x}\text{Rh}_x\text{O}_4$  ( $x=0, 0.01, 0.03$  and  $0.05$ ), (a)  $x=0$ , (b)  $x=0.01$ , (c)  $x=0.03$  and (d)  $x=0.05$ .

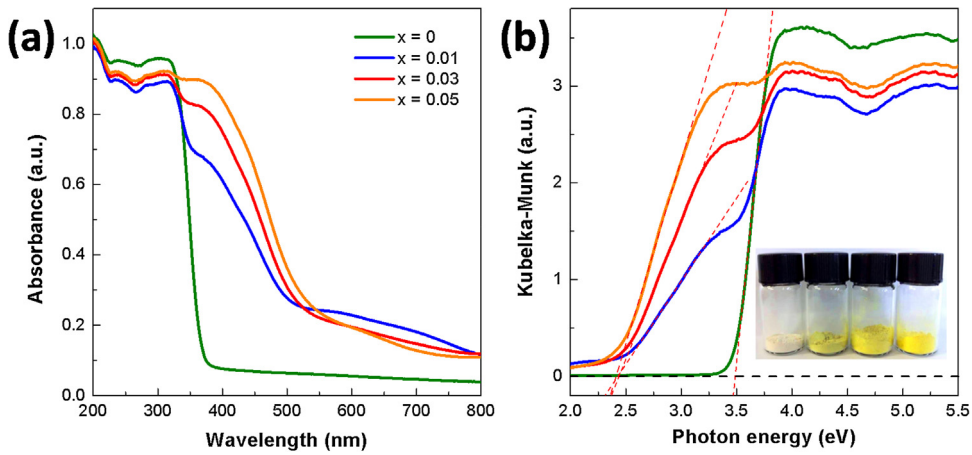


**Fig. 4.** (a) UV–vis light absorption spectra (converted from diffuse reflectance spectra) of as-prepared samples  $\text{Sr}_{2-x}\text{La}_x\text{Ti}_{1-x}\text{Rh}_x\text{O}_4$  ( $x=0, 0.01, 0.03$  and  $0.05$ ) and (b) Kubelka–Munk transformation of diffuse reflectance data. A digital photograph of all sample powders is inserted (doping level increases from left to right).

are not detected, confirming the effectiveness of La for balancing the charge. The absence of La/Rh signals for lightly doped samples ( $x=0.01$ ) is probably due to the detecting limit of XPS techniques that only contain information of very top surface ( $\sim 3$  nm) [80]. It is interesting to see that Rh singly doped  $\text{Sr}_2\text{TiO}_4$  does not give a clear Rh signal as well even though it has a high Rh doping level (3% Rh

doping), suggesting that La have an important role in holding Rh at the surface of  $\text{Sr}_2\text{TiO}_4$  (Fig. S5).

### 3.5. Photocatalytic hydrogen production

The photocatalytic properties of as-prepared samples were then evaluated by monitoring the hydrogen evolution from aqueous

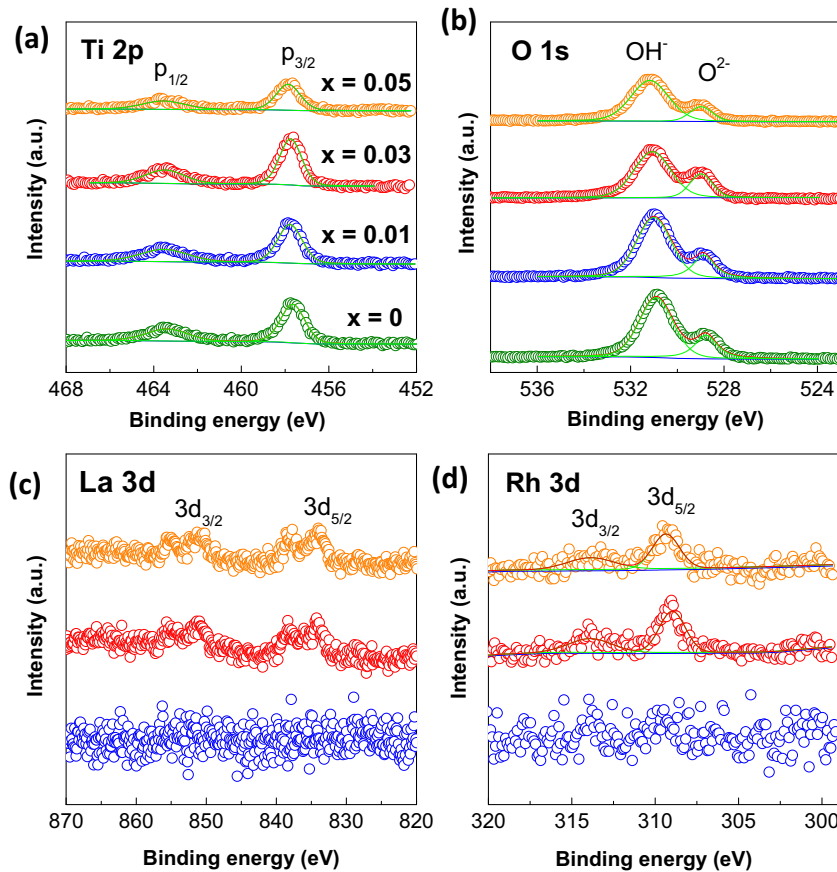


Fig. 5. XPS spectra of constituent elements of  $\text{Sr}_{2-x}\text{Lax}\text{Ti}_{1-x}\text{Rh}_x\text{O}_4$  ( $x = 0, 0.01, 0.03$  and  $0.05$ ): (a) Ti 2p, (b) O 1s, (c) La 3d and (d) Rh 3d.

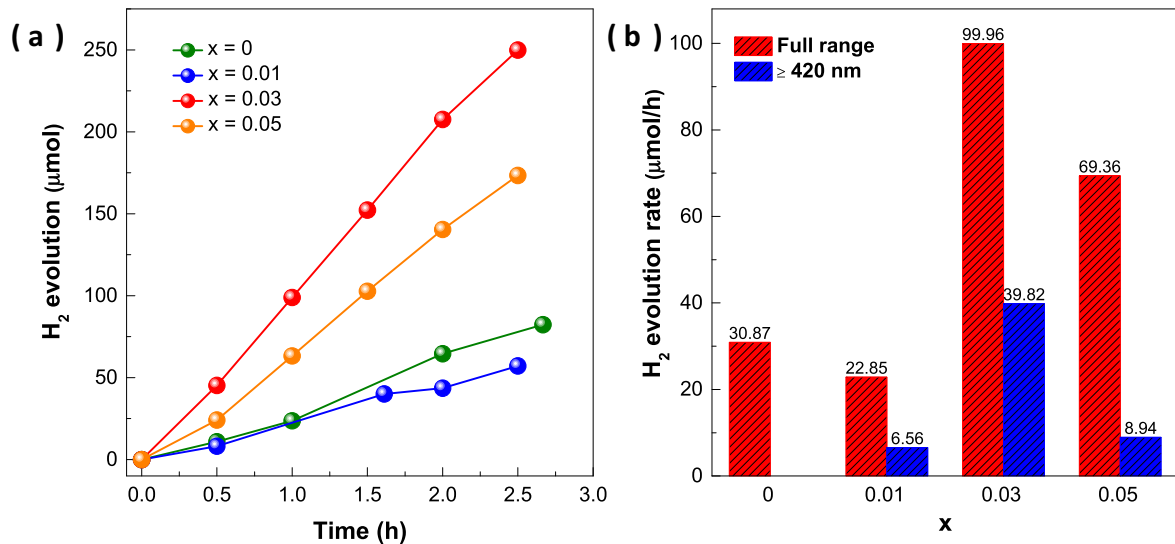


Fig. 6. (a) Photocatalytic hydrogen production of freshly prepared samples  $\text{Sr}_{2-x}\text{Lax}\text{Ti}_{1-x}\text{Rh}_x\text{O}_4$  ( $x = 0, 0.01, 0.03$  and  $0.05$ ) under full range irradiation ( $\lambda \geq 250 \text{ nm}$ ) in sodium sulfite aqueous solution (0.05 M) and (b) average photocatalytic hydrogen production rate under full range ( $\lambda \geq 250 \text{ nm}$ ) and visible light irradiation ( $\lambda \geq 420 \text{ nm}$ ).

solution under different irradiation conditions. Pt (1 wt%) was loaded as a co-catalyst and sodium sulfite (0.05 M) was used as a sacrificial agent to promote the photo-reduction reactions. Control experiments were carried out first either with light or sample powders absent to check any reactions that do not proceed photocatalytically. No  $\text{H}_2$  was detected for 5 h therefore precluding any reactions that will give rise to  $\text{H}_2$  evolution spontaneously. Steady hydrogen evolution was detected immediately

upon light irradiation, confirming a real photocatalytic process. Typical temporal hydrogen evolution under full range irradiation ( $\lambda \geq 250 \text{ nm}$ ) is illustrated in Fig. 6a. All samples demonstrate progressive hydrogen evolution during the whole irradiation period. La/Rh co-doped  $\text{Sr}_2\text{TiO}_4$  clearly display a much better photocatalytic activity than pristine one, suggesting the benefits of La/Rh co-doping. The only exception is  $\text{Sr}_{1.99}\text{La}_{0.01}\text{Ti}_{0.99}\text{Rh}_{0.01}\text{O}_4$  ( $x = 0.01$ ) which shows an activity slightly lower than pristine  $\text{Sr}_2\text{TiO}_4$ . The

highest activity belongs to  $\text{Sr}_{1.97}\text{La}_{0.03}\text{Ti}_{0.97}\text{Rh}_{0.03}\text{O}_4$  ( $x=0.03$ ) where more than  $250 \mu\text{mol}$  hydrogen were produced in total  $2.5 \text{ h}$ . This value is almost 3 times higher than pristine  $\text{Sr}_2\text{TiO}_4$ . The photocatalytic reactions for  $\text{Sr}_{1.97}\text{La}_{0.03}\text{Ti}_{0.97}\text{Rh}_{0.03}\text{O}_4$  ( $x=0.03$ ) was further extended to another  $7.5 \text{ h}$  with evacuation at each  $2.5 \text{ h}$  in order to check the stability of this sample. The hydrogen evolution continued at the whole experimental period with activity stabilized after  $5 \text{ h}$  (Fig. S7). More than  $850 \mu\text{mol}$  hydrogen was produced for the whole irradiation period ( $10 \text{ h}$ ), which exceeds the total amounts of catalyst used ( $171 \mu\text{mol}$ ). XRD patterns and XPS spectra of constituent elements before and after photocatalytic experiment remains the same (Figs. S8 and S9), suggesting the good stability of this compound. Therefore,  $\text{Sr}_{1.97}\text{La}_{0.03}\text{Ti}_{0.97}\text{Rh}_{0.03}\text{O}_4$  ( $x=0.03$ ) acts as an efficient photocatalyst for hydrogen production from water. More importantly, hydrogen production was also achieved under visible light irradiation ( $\lambda \geq 420 \text{ nm}$ ) for La/Rh co-doped  $\text{Sr}_2\text{TiO}_4$  and the averaged photocatalytic hydrogen production rates were plotted in Fig. 6b.  $\text{Sr}_{1.97}\text{La}_{0.03}\text{Ti}_{0.97}\text{Rh}_{0.03}\text{O}_4$  ( $x=0.03$ ) exhibit the highest activity both under full range and visible light irradiation among all samples. The hydrogen evolution rates approaches  $\sim 100 \mu\text{mol}/\text{h}$  and  $\sim 40 \mu\text{mol}/\text{h}$  for full range and visible light irradiation, corresponding to apparent quantum efficiency  $\sim 1.27\%$  and  $1.18\%$ . The importance of La/Rh as dopants can be realized by the fact that the activity of pristine  $\text{Sr}_2\text{TiO}_4$  under full range irradiation is exceeded by the activity of  $\text{Sr}_{1.97}\text{La}_{0.03}\text{Ti}_{0.97}\text{Rh}_{0.03}\text{O}_4$  ( $x=0.03$ ) under visible light irradiation (Fig. 6b). The necessity of La in the co-doping scheme was verified by the poor photocatalytic activity of Rh singly doped  $\text{Sr}_2\text{TiO}_4$  even at the same Rh doping level (Fig. S6). Surface area shall not play a dominant role here as they own comparable values (Table 1). It is interesting to see an optimal doping level for La/Rh co-doped  $\text{Sr}_2\text{TiO}_4$ , as higher doping level gives more visible light absorption. We then resort to photoelectrochemical techniques for further analysis.

### 3.6. Photoelectrochemical (PEC) investigations

First, we performed linear sweep voltammetry (LSV) measurements under chopped light irradiation for as-prepared photoelectrodes fabricated by sample powders. Clear anodic photocurrent can be easily identified for La/Rh co-doped  $\text{Sr}_2\text{TiO}_4$  under visible light irradiation (Fig. 7a), highlighting the usefulness of Rh in modifying visible light photocatalysis. The best photocatalytic activity observed previously for sample  $\text{Sr}_{1.97}\text{La}_{0.03}\text{Ti}_{0.97}\text{Rh}_{0.03}\text{O}_4$  ( $x=0.03$ ) can be understood by its highest photocurrent among all samples under both full range and visible light irradiation (Fig. 7). Besides a small photocurrent, the lightly doped sample  $\text{Sr}_{1.99}\text{La}_{0.01}\text{Ti}_{0.99}\text{Rh}_{0.01}\text{O}_4$  ( $x=0.01$ ) exhibit an onset potential for photocurrent at about  $-0.2 \text{ V}$  (vs NHE), which is more positive than those at higher doping levels ( $\sim -0.4 \text{ V}$  vs NHE). Such a stronger reliance on external bias for photocurrent generation clearly reflects the poor charge separation condition in this sample thus explains its low photocatalytic activity. Doping small amounts of Rh into  $\text{Sr}_2\text{TiO}_4$  probably introduces only isolated energy states, which are not favorable for fast charge migrations [68]. However, at high doping level ( $x=0.05$ ), the photocurrent remain small even though it has similar onset potential and strong light absorption. Close inspection of its LSV curve suggests that its photocurrent remains almost constant at high external bias, particularly under full range irradiation. The insensitivity of photocurrent to external bias implies that new factors are dominating the generation/extraction of photocurrent at high doping level ( $x=0.05$ ). One possible explanation is the increased charge recombination events at high doping level as dopants per se may act as charge trapping centers which counterbalances the positive effects of doping. Another possible explanation is surface modification which may prevent fast charge transfer from happening. Recent study on La

modified  $\text{NaTaO}_3$  suggests that La will block the surface catalytic site and hinder charge transfer [81]. Similar phenomenon may also occur here and a high La doping level would certainly decrease the performance.

The generation and subsequent consumption of photo-generated electrons inside semiconductors can be probed by monitoring the open-circuit voltage ( $V_{oc}$ ) of photoelectrodes in response to light illumination and termination [55,82,83].  $V_{oc}$  of photoelectrodes represent the voltage difference between Fermi level of semiconductor and counter electrode. For n-type semiconductors, illuminating the photoelectrode under open-circuit condition accumulates photo-generated electrons inside semiconductors as holes migrate to the surface and are consumed during photo-oxidation reactions [84]. This effectively shifts Fermi level of semiconductors negatively, so does  $V_{oc}$ . Steady state  $V_{oc}$  will be reached as long as electron consumption competes with electron accumulation. Instantaneously terminating illumination of photoelectrodes results in decay of  $V_{oc}$  which is controlled by various electron dissipation pathways (e.g. recombined with trapped holes). This provides a direct evaluation of charge separation and recombination conditions inside semiconductors. The lifetime of those accumulated electrons can be quantitatively approximated using the following equation [82,83]:

$$\tau_n = \frac{k_B T}{e} \left( \frac{dV_{oc}}{dt} \right)^{-1} \quad (1)$$

where  $\tau_n$  is potential dependent lifetime,  $k_B$  is Boltzmann's constant,  $T$  is the temperature in K and  $e$  is the elementary charge. Fig. 8 illustrates the  $V_{oc}$  time profile of all doped samples. Negative shifting  $V_{oc}$  occurred immediately upon light illumination, confirming the accumulation of electrons. However, steady state  $V_{oc}$  was not reached for all samples during the entire illumination period ( $100 \text{ s}$ ), likely due to the sluggish photo-oxidation reactions at the surface which did not rapidly drain holes. Apparently,  $\text{Sr}_{1.97}\text{La}_{0.03}\text{Ti}_{0.97}\text{Rh}_{0.03}\text{O}_4$  ( $x=0.03$ ) give the most negative shift of  $V_{oc}$ , attributable to the most photo-generated charges inside. Decay of  $V_{oc}$  occurred instantly upon light termination but at different speeds among samples. Lightly doped  $\text{Sr}_2\text{TiO}_4$  ( $x=0.01$ ) decayed in the fastest speed which took about  $150 \text{ s}$  for  $V_{oc}$  restoring back to its dark value. This indicates rapid charge recombination events occurring inside the sample and explains its poor photocatalytic activity. Likewise,  $\text{Sr}_{1.97}\text{La}_{0.03}\text{Ti}_{0.97}\text{Rh}_{0.03}\text{O}_4$  ( $x=0.03$ ) demonstrated the longest decay time ( $\sim 650 \text{ s}$ ), being consistent with its highest photocurrent and best photocatalytic activity. Further increasing the doping level to  $x=0.05$  decreases the decay time to about  $350 \text{ s}$ , as expected for this sample. The calculated electron lifetime was plotted in Fig. 8b, which clearly emphasizes the long lived electrons in sample  $\text{Sr}_{1.97}\text{La}_{0.03}\text{Ti}_{0.97}\text{Rh}_{0.03}\text{O}_4$  ( $x=0.03$ ). All these data agrees well with photocatalytic performance of these samples.

The band edge positions of all samples were then evaluated by electrochemical method. Fig. 9 displays the Mott-Schottky (MS) plot for all photoelectrodes. The positive slopes of MS curves as well as anodic photocurrent during PEC measurements suggest n-type semiconductivity. The flat band potential was then determined by extrapolating the linear region of MS curve down to the potential axis, which read to be  $-0.61 \text{ V}$ ,  $-0.65 \text{ V}$ ,  $-0.69 \text{ V}$  and  $-0.66 \text{ V}$  for  $x=0, 0.01, 0.03$  and  $0.05$ , respectively. Accordingly, the band edge positions (i.e. conduction band (CB) and valence band (VB) edges) can be easily inferred with the aid of UV-vis spectra data and are plotted in Fig. 9b. As can be seen from this plot, all samples essentially have similar CB edges and La/Rh co-doping effectively uplifts the VB band edge by about  $1 \text{ V}$ .

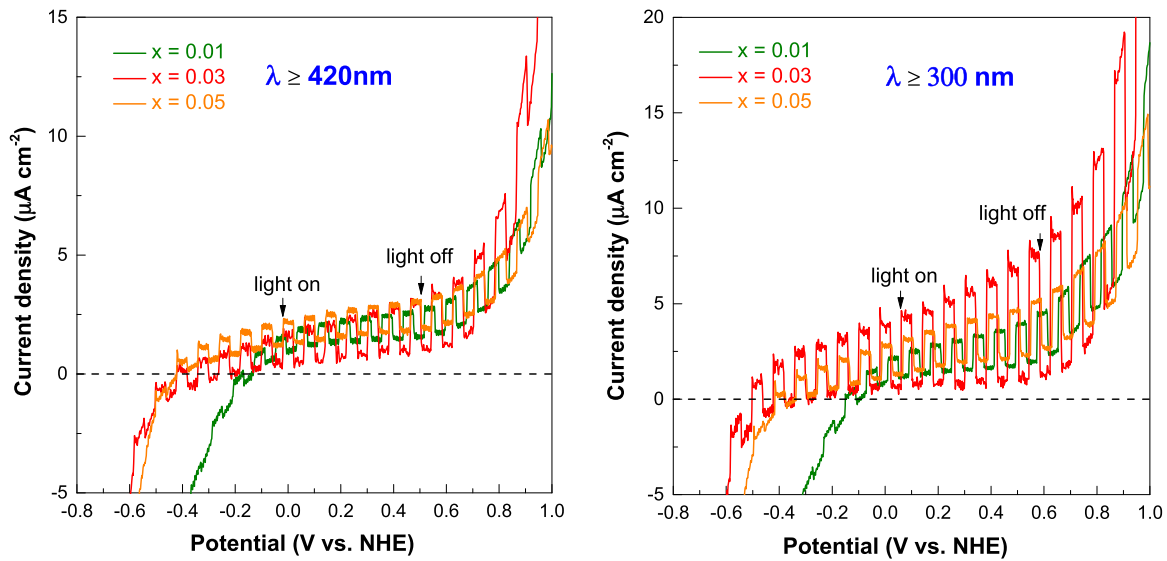


**Fig. 7.** Linear sweep voltammetry (LSV) of freshly prepared photoelectrodes fabricated by samples  $\text{Sr}_{2-x}\text{La}_x\text{Ti}_{1-x}\text{Rh}_x\text{O}_4$  ( $x = 0.01, 0.03$  and  $0.05$ ) powders under chopped light irradiation under (a) visible light irradiation ( $\lambda \geq 420 \text{ nm}$ ) and (b) UV-vis light irradiation ( $\lambda \geq 300 \text{ nm}$ ).

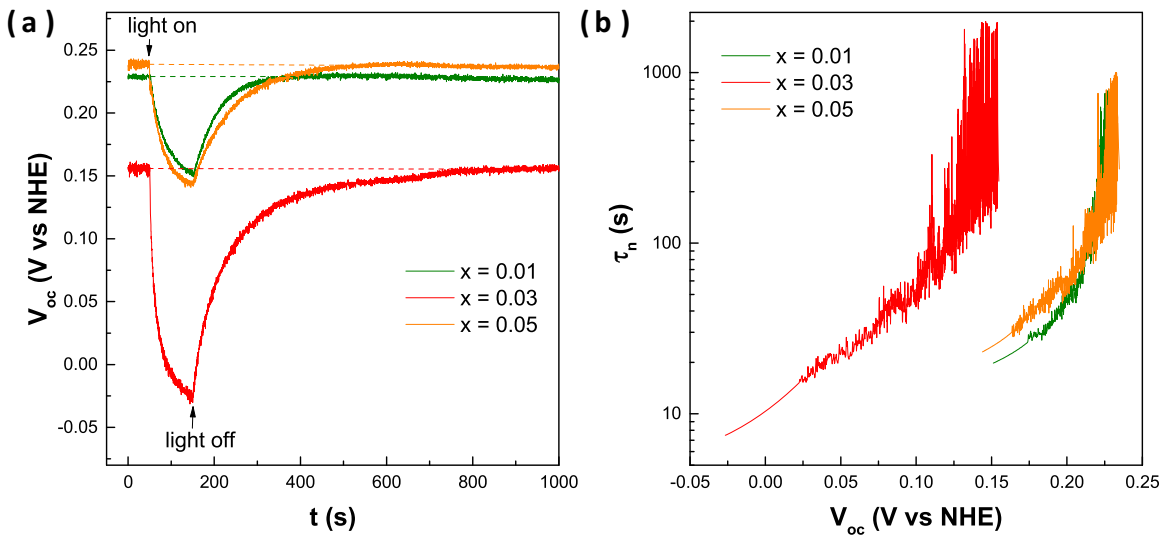


**Fig. 8.** (a)  $V_{oc}$  time profile of  $\text{Sr}_{2-x}\text{La}_x\text{Ti}_{1-x}\text{Rh}_x\text{O}_4$  ( $x = 0.01, 0.03$  and  $0.05$ ) in Ar atmosphere, irradiation ( $\lambda \geq 420 \text{ nm}$ ) started after a steady  $V_{oc}$  was achieved in the dark and was terminated after 100 s, (b) the electron lifetime derived from Eq. (1).

### 3.7. Theoretical calculations

For better understanding the origin of all changes induced by La/Rh co-doping, we carried out theoretical calculations on the electronic structures of  $\text{Sr}_2\text{TiO}_4$  with La/Rh randomly incorporated. The calculated band structures and density of states (DOS) are illustrated in Fig. 10. As can be seen from the band structures, a direct band gap of  $\sim 0.6 \text{ eV}$  is clearly seen at  $\Gamma$  point, confirming the semi-conductivity of this compound. This calculated band gap value is significantly smaller than the experimental one ( $\sim 2.4 \text{ eV}$ ), probably due to the drawbacks of the generalized gradient approximation (GGA) method that often underestimates the band gaps [85]. Nevertheless, the calculation can be used qualitatively. Analysis of density of states for individual band reveals that the CB is mainly composed of Ti 3d orbitals while VB is dominated by Rh 4d orbitals. The band involving mainly O 2p orbitals that typically forms VB of pristine  $\text{Sr}_2\text{TiO}_4$  and other oxide semiconductors lies approximately 1 eV lower than Rh 4d band. This agrees quite well with electrochemical analysis of the band edge positions that La/Rh co-doping uplifts the

VB edge of  $\text{Sr}_2\text{TiO}_4$  by about 1 V. Therefore, the reduced band gap and thereafter the visible light absorption and photocatalytic activity of La/Rh co-doped  $\text{Sr}_2\text{TiO}_4$  stems from the formation of this new VB inside the original band gap of  $\text{Sr}_2\text{TiO}_4$ . More interestingly, close examination of the band structure suggests anisotropic features for charge migrations. Take CB for instance, the band dispersion from point  $\Gamma$  to point X controls the electron migration along [100] direction, which spreads an energy range of more than 1 eV. This is not the case however from point M to point A, which governs the electron migration along [001] direction, being nearly zero energy dispersion (band pins). Similar observation can be also noticed for VB. It is known that the effective mass ( $m^*$ ) of charge carriers (electrons or holes) is proportional to the second derivatives of  $E$  versus  $k$  curve (i.e. wide band gives small  $m^*$ ) [86,87]:

$$m^* = \hbar^2 \left( \frac{d^2 E}{dk^2} \right)^{-1} \quad (2)$$

Presumably, the  $m^*$  for the charge migration along [001] is enormously large. Thereby, charge migrations are essentially forbidden

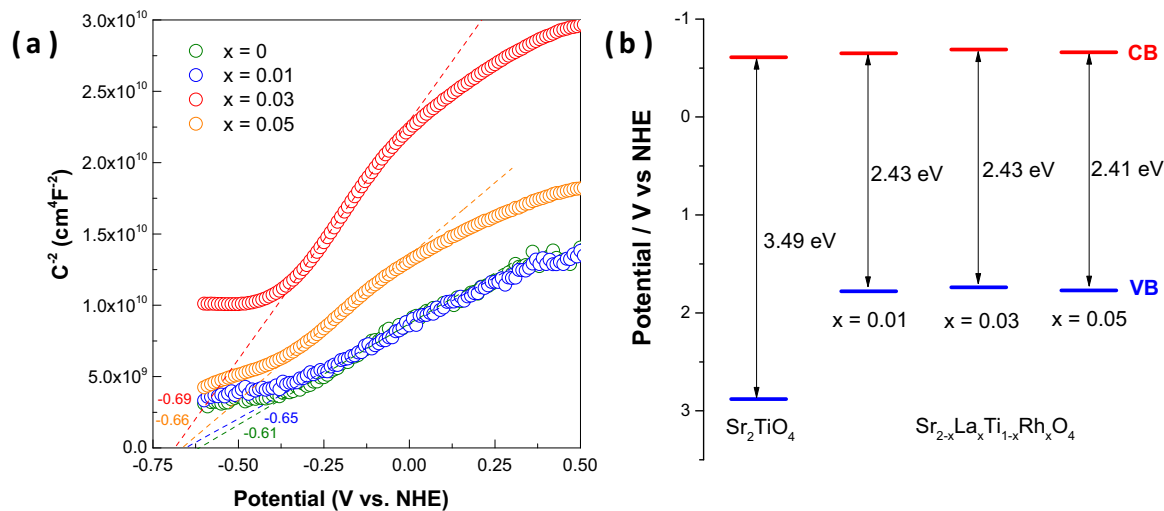


**Fig. 9.** (a) Mott-Schottky plot of freshly prepared photoelectrode fabricated from  $\text{Sr}_{2-x}\text{La}_x\text{Ti}_{1-x}\text{Rh}_x\text{O}_4$  ( $x = 0, 0.01, 0.03$  and  $0.05$ ) sample powders, capacitance was extracted from the impedance analysis at fixed frequency of 1000 Hz with 10 mV amplitude, (b) schematic representation of band edge positions of all samples.

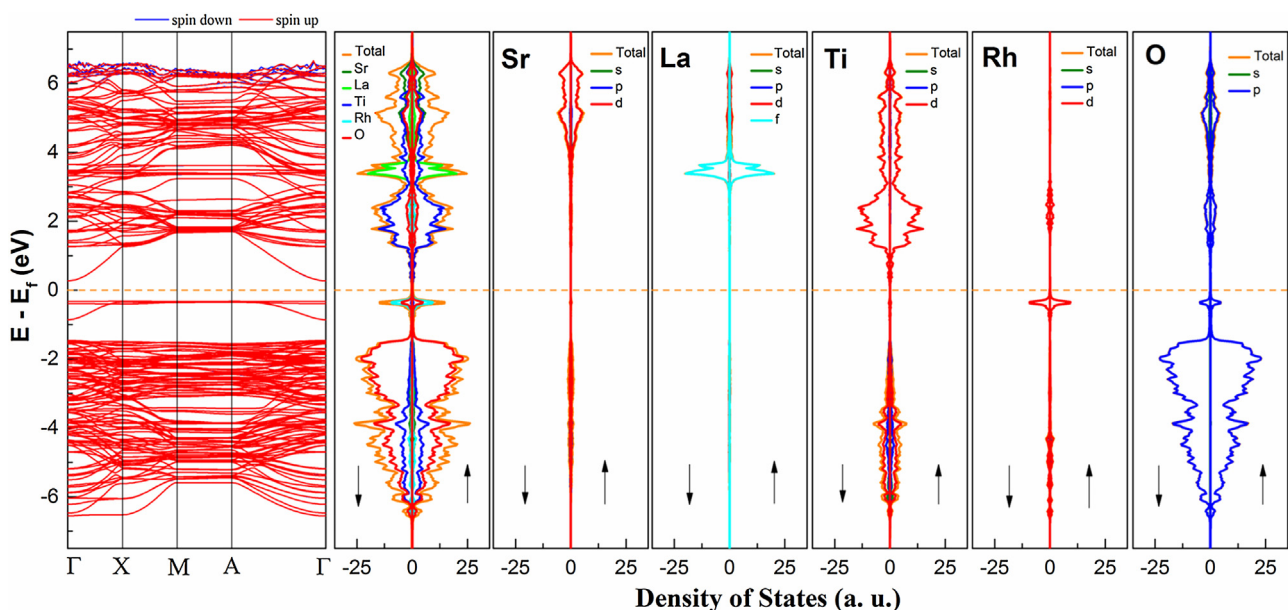


**Fig. 10.** Calculated band structure, total density of states (DOS) and partial density of states (PDOS) of constituent elements for La/Rh co-doped  $\text{Sr}_2\text{TiO}_4$ .

along [001] direction but are allowed in all directions that are perpendicular to [001] direction. Recall the fact that CB and VB is dominated by Ti 3d and Rh 4d/0 2p orbitals. Charge migrations, therefore, are confined within individual  $\text{Ti}(\text{Rh})\text{O}_6$  octahedron layer (intralayer migration) and migration between neighboring layers are prohibited (interlayer migration). This is highly beneficial for photocatalytic reactions as charge recombination events among different layers are effectively avoided. Similar observation has also been noticed in a number of layered compounds [41,64,88], signifying the impact of structural lamination upon charge transportation.

In light of all above results and analysis, it is now worthwhile to discuss optical and photocatalytic properties of  $\text{Sr}_2\text{TiO}_4$  in terms of La/Rh co-doping. As is schematically represented in Fig. 11, the pristine  $\text{Sr}_2\text{TiO}_4$  is characterized by wide separation of CB and VB (VB2 in Fig. 11), which can be only excited by UV photons and hence exhibit only UV light photocatalytic activity. Co-doping La/Rh into  $\text{Sr}_2\text{TiO}_4$  introduces additional VB (VB1) into the band gap of pristine  $\text{Sr}_2\text{TiO}_4$  which significantly reduces the threshold of photon excitation and is responsible for the visible light photocatalytic activity.

The relatively poor activity under visible light irradiation might be due to the narrow Rh 4d band that is not favorable for hole transportation.

#### 4. Conclusions

We have successfully prepared a series of La/Rh co-doped  $\text{Sr}_2\text{TiO}_4$  via a polymerized-complex method. Single phase compound were achieved at a calcination temperature as low as 900 °C. Introducing La/Rh into  $\text{Sr}_2\text{TiO}_4$  slightly expands its crystal structure and the layered architecture is maintained. The band gap of  $\text{Sr}_2\text{TiO}_4$  is significantly reduced upon co-doping La/Rh, which is responsible for the strong visible light absorption and yellowish appearance of sample powders. All doped Rh in  $\text{Sr}_2\text{TiO}_4$  remains in low oxidation state ( $\text{Rh}^{3+}$ ) and is likely due to the presence of La that builds a charge balanced system. Efficient photocatalytic hydrogen production was observed for these La/Rh co-doped  $\text{Sr}_2\text{TiO}_4$  both under full range ( $\lambda \geq 250 \text{ nm}$ ) and visible light irradiation ( $\lambda \geq 420 \text{ nm}$ ). The highest photocatalytic activity

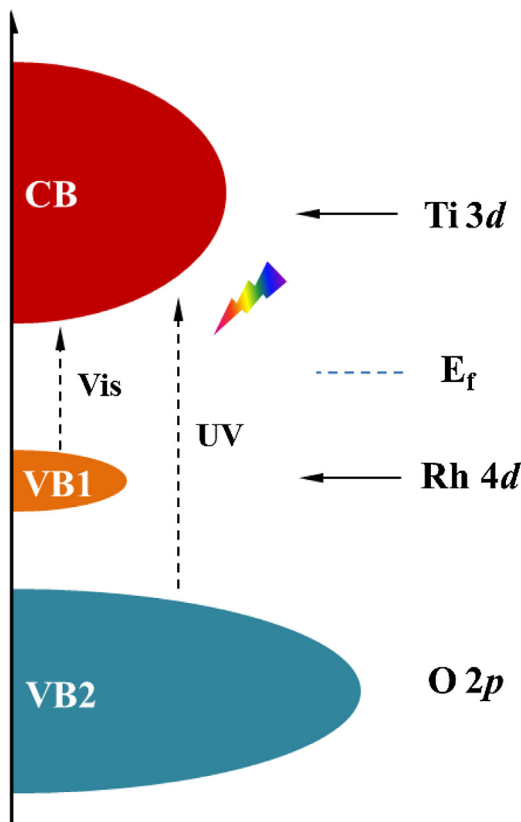


**Fig. 11.** Schematic representation of band structures of La/Rh doped  $\text{Sr}_2\text{TiO}_4$  and possible charge generation routes; the Fermi level is marked by the dotted line. VB1 denotes newly formed valence band from Rh 4d orbitals and VB2 denotes valence band from O 2p orbitals.

belongs to  $\text{Sr}_{1.97}\text{La}_{0.03}\text{Ti}_{0.97}\text{Rh}_{0.03}\text{O}_4$  ( $x = 0.03$ ) which gives average hydrogen production rate  $\sim 100 \mu\text{mol}/\text{h}$  and  $\sim 40 \mu\text{mol}/\text{h}$  under full range ( $\lambda \geq 250 \text{ nm}$ ) and visible light irradiation ( $\lambda \geq 420 \text{ nm}$ ), corresponding to apparent quantum efficiency of  $\sim 1.27\%$  and  $1.18\%$ , respectively. The optimal doping level for photocatalytic activity may origin from the strong dependence of charge separation and electron lifetime upon Rh level. Mott-Schottky analysis and theoretical calculation suggest that the band gap reduction in La/Rh co-doped  $\text{Sr}_2\text{TiO}_4$  stems from the formation of new valance band with Rh 4d character which uplifts the valence band edge and is responsible for the visible light photocatalytic activity. The impact of structural lamination in  $\text{Sr}_2\text{TiO}_4$  can be realized by the confined charge migrations within individual  $\text{TiO}_6$  octahedron layer.

## Acknowledgments

We thank Young Scientists Fund of the National Natural Science Foundation of China (Grant No. 21401142) for funding and Recruitment Program of Global Youth Experts (1000 plan). The work was supported by Shanghai Science and Technology Commission (14DZ2261100) and the Fundamental Research Funds for the Central Universities.

## Appendix A. Supplementary data

Supplementary data associated with this article can be found, in the online version, at <http://dx.doi.org/10.1016/j.apcatb.2017.03.063>.

## References

- B. Dudley, BP Statistical Review of World Energy June 2014, 2014.
- D.G. Nocera, Chem. Soc. Rev. 38 (2009) 13–15.
- N.S. Lewis, D.G. Nocera, Proc. Natl. Acad. Sci. U. S. A. 103 (2006) 15729–15735.
- R.C. Armstrong, Nat. Energy 1 (2016) 1–8.
- M.R. Hoffmann, S.T. Martin, W.Y. Choi, D.W. Bahnemann, Chem. Rev. 95 (1995) 69–96.
- X.X. Xu, C. Randorn, P. Efstratiou, J.T.S. Irvine, Nat. Mater. 11 (2012) 595–598.
- K. Maeda, K. Teramura, D.L. Lu, T. Takata, N. Saito, Y. Inoue, K. Domen, Nature 440 (2006) 295–295.
- A. Fujishima, K. Honda, Nature 238 (1972) 37–38.
- F.T. Wagner, G.A. Somorjai, Nature 285 (1980) 559–560.
- Z.G. Zou, J.H. Ye, K. Sayama, H. Arakawa, Nature 414 (2001) 625–627.
- A. Listorti, J. Durrant, J. Barber, Nat. Mater. 8 (2009) 929–930.
- X.C. Wang, K. Maeda, A. Thomas, K. Takanabe, G. Xin, J.M. Carlsson, K. Domen, M. Antonietti, Nat. Mater. 8 (2009) 76–80.
- K.F. Zhang, Y.X. Liu, J.G. Deng, S.H. Xie, H.X. Lin, X.T. Zhao, J. Yang, Z. Han, H.X. Dai, Appl. Catal. B: Environ. 202 (2017) 569–579.
- K.M. Ji, H. Arandiyani, P. Liu, L. Zhang, J.H. Han, Y.C. Xue, J.G. Hou, H.X. Dai, Nano Energy 27 (2016) 515–525.
- K.M. Ji, H.X. Dai, J.G. Deng, H.J. Zang, H. Arandiyani, S.H. Xie, H.G. Yang, Appl. Catal. B: Environ. 168 (2015) 274–282.
- K.M. Ji, J.G. Deng, H.J. Zang, J.H. Han, H. Arandiyani, H.X. Dai, Appl. Catal. B: Environ. 165 (2015) 285–295.
- H.Y. Jiang, H.X. Dai, X. Meng, K.M. Ji, L. Zhang, J.G. Deng, Appl. Catal. B: Environ. 105 (2011) 326–334.
- C.R. Cox, J.Z. Lee, D.G. Nocera, T. Buonassisi, Proc. Natl. Acad. Sci. U. S. A. 111 (2014) 14057–14061.
- Z.B. Chen, T.F. Jaramillo, T.G. Deutscher, A. Kleiman-Shwarzstein, A.J. Forman, N. Gaillard, R. Garland, K. Takanabe, C. Heske, M. Sunkara, E.W. McFarland, K. Domen, E.L. Miller, J.A. Turner, H.N. Dinh, J. Mater. Res. 25 (2010) 3–16.
- A. Kudo, Y. Miseki, Chem. Soc. Rev. 38 (2009) 253–278.
- X.B. Chen, S.H. Shen, L.J. Guo, S.S. Mao, Chem. Rev. 110 (2010) 6503–6570.
- M.G. Walter, E.L. Warren, J.R. McKone, S.W. Boettcher, Q.X. Mi, E.A. Santori, N.S. Lewis, Chem. Rev. 110 (2010) 6446–6473.
- R. Asahi, T. Morikawa, T. Ohwaki, K. Aoki, Y. Taga, Science 293 (2001) 269–271.
- B. Kiss, C. Didier, T. Johnson, T.D. Manning, M.S. Dyer, A.J. Cowan, J.B. Claridge, J.R. Darwent, M.J. Rosseinsky, Angew. Chem. Int. Ed. 53 (2014) 14480–14484.
- L.W. Lu, M.L. Lv, D. Wang, G. Liu, X.X. Xu, Appl. Catal. B: Environ. 200 (2017) 412–419.
- L.W. Lu, M.L. Lv, G. Liu, X.X. Xu, Appl. Surf. Sci. 391 (2017) 535–541.
- X.Q. Sun, S.W. Wang, C. Shen, X.X. Xu, ChemCatChem 8 (2016) 2289–2295.
- X.X. Xu, Y.H. Xie, S. Ni, A.K. Azad, T.C. Cao, J. Solid State Chem. 230 (2015) 95–101.
- H.H. Li, S. Yin, Y.H. Wang, T. Sekino, S.W. Lee, T. Sato, J. Catal. 297 (2013) 65–69.
- X.X. Xu, M.L. Lv, X.Q. Sun, G. Liu, J. Mater. Sci. 51 (2016) 6464–6473.
- R. Niishiro, H. Kato, A. Kudo, Phys. Chem. Chem. Phys. 7 (2005) 2241–2245.
- M.L. Lv, Y.H. Xie, Y.W. Wang, X.Q. Sun, F.F. Wu, H.M. Chen, S.W. Wang, C. Shen, Z.F. Chen, S. Ni, G. Liu, X.X. Xu, Phys. Chem. Chem. Phys. 17 (2015) 26320–26329.
- W.J. Luo, Z.S. Li, X.J. Jiang, T. Yu, L.F. Liu, X.Y. Chen, J.H. Ye, Z.G. Zou, Phys. Chem. Chem. Phys. 10 (2008) 6717–6723.
- R. Konta, T. Ishii, H. Kato, A. Kudo, J. Phys. Chem. B 108 (2004) 8992–8995.
- B. Modak, S.K. Ghosh, J. Phys. Chem. C 119 (2015) 7215–7224.
- S. Kawasaki, K. Akagi, K. Nakatsuji, S. Yamamoto, I. Matsuda, Y. Harada, J. Yoshinobu, F. Komori, R. Takahashi, M. Lippmaa, C. Sakai, H. Niwa, M. Oshima, K. Iwashina, A. Kudo, J. Phys. Chem. C 116 (2012) 24445–24448.
- B. Modak, S.K. Ghosh, J. Phys. Chem. B 119 (2015) 11089–11098.
- Q. Wang, T. Hisatomi, S.S.K. Ma, Y.B. Li, K. Domen, Chem. Mater. 26 (2014) 4144–4150.
- H. Kato, Y. Sasaki, N. Shirakura, A. Kudo, J. Mater. Chem. A 1 (2013) 12327–12333.
- Q. Wang, T. Hisatomi, Q.X. Jia, H. Tokudome, M. Zhong, C.Z. Wang, Z.H. Pan, T. Takata, M. Nakabayashi, N. Shibata, Y.B. Li, I.D. Sharp, A. Kudo, T. Yamada, K. Domen, Nat. Mater. 15 (2016), 611–.
- X.Q. Sun, Y.H. Xie, F.F. Wu, H.M. Chen, M.L. Lv, S. Ni, G. Liu, X.X. Xu, Inorg. Chem. 54 (2015) 7445–7453.
- K. Iwashina, A. Kudo, J. Am. Chem. Soc. 133 (2011) 13272–13275.
- R.H. Mitchell, *Peroxsites: Modern and Ancient*, Almaz Inc. Press, Ontario, Canada, 2002.
- B.V. Beznosikov, K.S. Aleksandrov, Crystallogr. Rep. 45 (2000) 792–798.
- J. Druce, T. Ishihara, J. Kilner, Solid State Ionics 262 (2014) 893–896.
- J. Druce, H. Tellez, M. Burriel, M.D. Sharp, L.J. Fawcett, S.N. Cook, D.S. McPhail, T. Ishihara, H.H. Brongersma, J.A. Kilner, Energy Environ. Sci. 7 (2014) 3593–3599.
- W. Jung, H.L. Tuller, Energy Environ. Sci. 5 (2012) 5370–5378.
- A.C. Lawson, A.C. Larson, M.C. Aronson, S. Johnson, Z. Fisk, P.C. Canfield, J.D. Thompson, R.B. Von Dreele, Los Alamos National Laboratory Report No. LA-UR-86-748 (1994).
- G. Kortum, W. Braun, G. Herzog, Angew. Chem. Int. Ed. Engl. 2 (1963) 333–341.
- P.V.d. Heide, *X-ray Photoelectron Spectroscopy—An Introduction to Principles and Practices*, John Wiley & Sons, Inc., Hoboken, 2012.
- H.M. Chen, Y.H. Xie, X.Q. Sun, M.L. Lv, F.F. Wu, L. Zhang, L. Li, X.X. Xu, Dalton Trans. 44 (2015) 13030–13039.
- M.L. Lv, S. Ni, Z. Wang, T.C. Cao, X.X. Xu, Int. J. Hydrogen Energy 41 (2016) 1550–1558.

[54] X.X. Xu, G. Liu, A.K. Azad, *Int. J. Hydrogen Energy* 40 (2015) 3672–3678.

[55] Y.H. Xie, Y.W. Wang, Z.F. Chen, X.X. Xu, *ChemSusChem* 9 (2016) 1403–1412.

[56] Y.W. Wang, D.Z. Zhu, X.X. Xu, *ACS Appl. Mater. Interfaces* 8 (2016) 35407–35418.

[57] G. Kresse, J. Furthmuller, *Phys. Rev. B* 54 (1996) 11169–11186.

[58] J.P. Perdew, K. Burke, M. Ernzerhof, *Phys. Rev. Lett.* 77 (1996) 3865–3868.

[59] G. Kresse, D. Joubert, *Phys. Rev. B* 59 (1999) 1758–1775.

[60] H.J. Monkhorst, J.D. Pack, *Phys. Rev. B* 13 (1976) 5188–5192.

[61] Z.G. Yi, H. Iwai, J.H. Ye, *Appl. Phys. Lett.* 96 (2010).

[62] J.Y. Wang, H. Zhou, J.T. Liu, S.Y. Jin, L.N. Sun, J.J. Zhang, *Ceram. Int.* 38 (2012) 3503–3507.

[63] K. Kawamura, M. Yashima, K. Fujii, K. Omoto, K. Hibino, S. Yamada, J.R. Hester, M. Avdeev, P. Miao, S. Torii, T. Kamiyama, *Inorg. Chem.* 54 (2015) 3896–3904.

[64] H.M. Chen, X.X. Xu, *Appl. Catal. B: Environ.* 206 (2017) 35–43.

[65] R.D. Shannon, C.T. Prewitt, *Acta Crystallogr. B* 25 (1969) 925–946.

[66] R.D. Shannon, C.T. Prewitt, *Acta Cryst. B* 26 (1970) 1046–1048.

[67] P.A. Cox, *The Electronic Structure and Chemistry of Solids*, University Press, Oxford, 1987.

[68] P.A. Cox, *Transition Metal Oxides: An Introduction to Their Electronic Structure and Properties*, Oxford University Press, 1992.

[69] H.G. Yang, C.H. Sun, S.Z. Qiao, J. Zou, G. Liu, S.C. Smith, H.M. Cheng, G.Q. Lu, *Nature* 453 (2008), 638–U634.

[70] Y.H. Xie, F.F. Wu, X.Q. Sun, H.M. Chen, M.L. Lv, S. Ni, G. Liu, X.X. Xu, *Sci. Rep.* 5 (2016) 19060.

[71] S. Kawasaki, K. Akagi, K. Nakatsuji, S. Yamamoto, I. Matsuda, Y. Harada, J. Yoshinobu, F. Komori, R. Takahashi, M. Lippmaa, C. Sakai, H. Niwa, M. Oshima, K. Iwashina, A. Kudo, *J. Phys. Chem. C* 116 (2012) 24445–24448.

[72] K. Iwashina, A. Kudo, *J. Am. Chem. Soc.* 133 (2011) 13272–13275.

[73] S. Okunaka, H. Tokudome, R. Abe, *J. Mater. Chem. A* 3 (2015) 14794–14800.

[74] K. Maeda, *ACS Appl. Mater. Interfaces* 6 (2014) 2167–2173.

[75] N. Kumagai, L. Ni, H. Irie, *Chem. Commun.* 47 (2011) 1884–1886.

[76] F.F. Wu, G. Liu, X.X. Xu, *J. Catal.* 346 (2017) 10–20.

[77] F.F. Wu, M.L. Lv, X.Q. Sun, Y.H. Xie, H.M. Chen, S. Ni, G. Liu, X.X. Xu, *CeramCatChem* 8 (2016) 615–623.

[78] M.L. Lv, Y.W. Wang, L.W. Lu, R.N. Wang, S. Ni, G. Liu, X.X. Xu, *Phys. Chem. Chem. Phys.* 18 (2016) 21491–21499.

[79] L. Schlapbach, H.R. Scherrer, *Solid State Commun.* 41 (1982) 893–897.

[80] P. Van der Heide, *X-ray Photoelectron Spectroscopy—An Introduction to Principles and Practices*, John Wiley & Sons, Inc, Hoboken, New Jersey, 2012.

[81] S.P. Phivilay, A.A. Puretzky, K. Domen, I.E. Wachs, *ACS Catal.* 3 (2013) 2920–2929.

[82] B.H. Meekins, P.V. Kamat, *ACS Nano* 3 (2009) 3437–3446.

[83] A. Zaban, M. Greenshtein, J. Bisquert, *ChemPhysChem* 4 (2003) 859–864.

[84] J.A. Turner, *J. Chem. Educ.* 60 (1983) 327–329.

[85] H. Xiao, J. Tahir-Kheli, W.A. Goddard, *J. Phys. Chem. Lett.* 2 (2011) 212–217.

[86] C. Kittel, *Introduction to Solid State Physics*, 7th ed., Wiley, New York, 1996.

[87] H. Mizoguchi, P.M. Woodward, *Chem. Mater.* 16 (2004) 5233–5248.

[88] M.L. Lv, G. Liu, X.X. Xu, *ACS Appl. Mater. Interfaces* 8 (2016) 28700–28708.